Materials Horizons

ROYAL SOCIETY OF CHEMISTRY

COMMUNICATION

View Article Online
View Journal

Check for updates

Cite this: DOI: 10.1039/d5mh02460a

Received 27th December 2025,
Accepted 8th May 2026

DOI: 10.1039/d5mh02460a

rsc.li/materials-horizons

Slippery when charged: hydration lubrication in hydrogels

Ming Jun Lee,[a] Isha Bordawekar[a] and Rosa M. Espinosa-Marzal*[ab]

Hydrogels are hydrated polymer networks with promising biomedical applications due to their microstructural similarity to biological tissues at sliding interfaces, such as the articular cartilage. These tissues are highly hydrated, charged, and operate in ionic environments. A fundamental understanding of lubrication at charged hydrogel interfaces is thus essential to advance practical applications. Hydration lubrication has recently been proposed to govern hydrogel lubrication. Here, a thin film of water remains confined under pressure, enabling friction coefficients below 0.01, a condition referred to as superlubricity. Yet, studies of hydration lubrication in hydrogels remain limited. This work investigates positively charged polyvinyl alcohol–chitosan double-network hydrogels as a model system for hydrophilic, positively charged hydrogels. When equilibrated in salt solution, these hydrogels exhibit stronger surface zeta potential and weaker storage modulus. Using atomic force microscopy, we directly image the sliding interface in water and salt solutions while measuring friction with a negatively charged probe. Friction coefficients are highest in water and smallest in NaI solution. The results reveal that hydration (repulsive) forces can dominate over electrostatic attraction and activate superlubricity. This study provides new insights into the mechanisms that govern hydration lubrication in charged hydrogels.

New concepts

Soft material interfaces are ubiquitous in biological tissues. These tissues are hydrated, charged, and immersed in ionic environments. Hydrogels—hydrated polymer networks—closely mimic these characteristics, making them model systems for probing interfacial behavior. Fundamental knowledge of how these surfaces slide in contact is essential to understanding how pain arises from friction or to reduce wear using biocompatible gels. Distinct from prior work, we discover that, despite electrostatic attraction of an oppositely charged hydrogel surface, hydration forces can dominate and endow superlubricity (coefficient of friction <0.01). This effect is enhanced in ionic environments relative to water, with subtle anion-specific effects, as NaI can outperform NaCl. Analysis of the velocity-dependence of friction indicates that hydration lubrication governs hydrogel superlubricity, provided that the hydration repulsion is sufficiently strong. Increasing the ionic strength effectively charges the hydrogels and amplifies this repulsive interaction. Furthermore, the velocity dependence is modulated by the contact size, suggesting a dynamic regulation mechanism of the lubricating film thickness governed by fast rehydration during sliding.

1. Introduction

Many soft tissues function in the human body as natural hydrogels—highly hydrated polymer networks stabilized by ionic, hydrophobic, or hydrogen-bond interactions. These biological hydrogels are characterized by their softness, charge, visco- and poro-elasticity. These properties enable key functions, including lubrication, organ hydration and protection, and, in some cases, also mechanical load support. Synthetic hydrogels are designed to mimic these features, enabling applications in biomedical devices,[1] tissue engineering,[2] and soft robotics.[3] Despite their promise for diverse applications,[4] the fundamental understanding of structure–lubrication relationships remains limited.

Numerous studies have explored lubrication mediated by hydrophilic polymers in aqueous environments, with various mechanisms being proposed. Among these, hydration lubrication is widely considered most prevalent and broadly relevant and believed to play a crucial role in achieving superlubricity and minimizing wear in biological systems such as the ocular epithelium and articular joints. Hydration lubrication was originally proposed by Raviv and Klein to explain the lubrication of two negatively charged mica surfaces by a thin film of water containing dissolved salt.[5] In aqueous environments, oppositely charged ions–counterions, in this case cations–bind to the charged sites on mica to neutralize the surface charge, while retaining water molecules in their hydration shells. Their results confirmed that the Na-bound water molecules confined

---

[a] Department of Materials Science and Engineering, University of Illinois Urbana-Champaign, IL 61801, USA. E-mail: rosae@illinois.edu
[b] Department of Civil and Environmental Engineering, University of Illinois Urbana-Champaign, IL 61801, USA

between the mica surfaces remain fluid and exhibit low viscosity under shear, leading to friction coefficients μ in the order of 10^{-3}, thereby achieving superlubricity –*i.e.*, $\mu < 0.01$.[5,6] This concept was later extended to charged polymers tethered to surfaces–polyelectrolyte brushes– where friction coefficients as low as $\mu \sim 6.10^{-4}$ were measured under applied pressures up to 0.3 MPa using a surface force balance (SFB). However, multiple mechanisms contributed to the observed low friction, including the repulsive osmotic pressure arising from counterions within the brush film –so called, Donnan osmotic pressure.[7] Later, Chen and co-workers studied phosphorylcholine brushes, which contain both positively and negatively charged groups, making them overall neutral in order to eliminate the contribution from Donnan osmotic pressure differences. In this system, friction reduction was attributed solely to shearing the hydration shells surrounding the zwitterionic groups—which was considered to be a manifestation of pure hydration lubrication.[8,9] The friction coefficient remained low and approximately constant ($\mu \sim 4.10^{-4}$) across a range of sliding velocities (2–4000 nm s^{-1}) and pressures (0.3–7.5 MPa), supporting the conclusion that the absence of velocity dependence is a characteristic feature of hydration lubrication. Hydration lubrication has recently been invoked to explain lubrication in hydrogels with incorporated liposomes or grafted polymer brushes,[9–11] yet fundamental studies are still scarce.

The velocity-dependence of hydrogel friction is complex. The seminal work by Gong *et al.*[12] proposed that the very strong hydration ability of hydrogels makes it possible to sustain hydrodynamic lubrication, even at low sliding velocity – yet generally higher than in SFB studies – and pressures up to ∼0.5 MPa on repulsive contacts. A prediction based on hydrodynamics led to $F \sim V^n$, with $n = 1$, as in experiments, but underestimated the friction force. Subsequent studies showed the increase of n from 0 to 0.55 with increasing load, and that friction could evolve from velocity-independent to velocity-dependent with increasing velocity.[13] According to soft elastohydrodynamic lubrication (EHL) theory, friction (F) arises from shear of the interfacial fluid film

$$F = \eta A \frac{V}{h} \tag{1}$$

where η, is the fluid viscosity, A the contact area, and h the film thickness. Hamrock & Dowson[14] observed that $h \propto V^{0.65}$, which would lead to $F \propto V^{0.35}$. Variations of this model can yield a range of exponents ($n \sim 0.3$–1), consistent with experimental observations.[12,15–18] Nonetheless, models underestimate friction, prompting the suggestion of non-Newtonian behavior of interfacial water, albeit without explicit modeling.[19]

Velocity-independent low friction has been observed for Gemini hydrogel interfaces in tribometer experiments. Gombert *et al.* showed that polyacrylamide hydrogels molded against a hydrophobic surface terminate in a brush-like layer that is able to retain an interfacial water film even under load.[20] When subjected to transient normal load and shear, water is exudated but the interface can easily rehydrate during the out-of-contact phase. This dynamic balance between exudation and rehydration enables the formation of a thick water film. By invoking hydrodynamic lubrication, this thick fluid film reduces shear stress and, consequently, the frictional force, resulting in low, quasi velocity-independent friction. In contrast, when molded against a hydrophilic surface, the hydrogel surface is well crosslinked, and cannot maintain an interfacial fluid film under load. The increase in friction with velocity, $F \sim V^{0.5-0.7}$, was associated with the existence of a thin fluid film that yields higher friction based on EHL. Instead, Sawyer's group associated velocity-independent friction with thermal-fluctuation lubrication.[16,21] That is the polymer chains create a dynamically blurred interface that can relax the shear stress through random thermal fluctuations, effectively reducing the energy barrier to sliding compared to a rigid interface. The transition to velocity-dependent friction ($\propto V^{0.5}$) at higher velocities could not be rationalized as EHL which predicted much lower friction forces. Here, the dissipation was attributed to the relaxation of strained polymer chains at the contact. Friction measurements by Atomic Force Microscopy have also revealed that the polymer network can contribute to dissipation, particularly at adhesive interfaces, where direct polymer–probe interactions and deformation of the network enhance energy dissipation beyond purely fluid-mediated lubrication.[17,22]

Pressure-driven fluid flow in hydrogels occurs when the applied pressure exceeds the osmotic pressure of the network, and water is pushed through the polymer network, a condition that generally requires the use of rigid probes.[23] The hallmark of poroelastically-driven lubrication is the decrease in friction with increasing sliding velocity, as the time available for fluid drainage is reduced and the contact area gradually decreases. Reale and Dunn's model[24] modelled the friction coefficient as a function of the Péclet number and the interfacial energy. Within this framework, decreasing velocity promotes dehydration of the contact, leading to an increase in adhesion energy with the countersurface and, consequently, higher friction. However, pressure-driven fluid flow can also lead to an increase in friction with velocity at sufficiently small sliding velocities, while the contact area remains constant.[23]

This work focuses on hydrogels composed of uncharged polyvinyl alcohol (PVA), which contains hydroxyl groups that make them highly hydrophilic, combined with chitosan (Cs), which carries amine groups that provide a positive charge in the selected pH range,[25] forming a double-network hydrogel. Double-network (DN) hydrogels – pioneered by Gong[26]– have emerged as an alternative to single-network (SN) hydrogels, because they are stronger and tougher and mimic better the properties of tissues like cartilage, tendon or blood vessels.[27] The two networks are usually chemically independent and physically entangled. Entanglement creates a synergistic effect where one network takes on load-bearing while the other provides ductility, together resulting in multifold strengthening over their individual SN hydrogels.[26] The charged nature of the double network introduces responsive behavior to added salts, which is leveraged here to probe the underlying lubrication mechanisms. The countersurface (silicon oxide) is negatively charged, resulting in electrostatic attraction between charged hydrogel and the solid surface. This work demonstrates that hydration repulsion can overcome electrostatic attraction and activate superlubricity and reveals subtle anion-specific effects. We further show that hydrogel friction under hydration lubrication can exhibit velocity dependence and propose a regulation mechanism of the film thickness to explain these results.

2. Experimental

2.1. Materials

Polyvinyl alcohol (341584), chitosan (448869), acetic acid (695092), sodium sulfate (238597), and sodium chloride (S9625) were used as received from Sigma Aldrich. Sodium iodide (7681-82-5) was used as received from Fluka. 5 μm silica colloids (SS05003) were used as received from Bangs Laboratories.

2.2. Hydrogel preparation

Polyvinyl alcohol/chitosan double network hydrogels were prepared *via* a two-step synthesis method that involved freeze–thaw and ionic cross-linking. Polyvinyl alcohol (PVA) was dissolved in water and acetic acid (acetic acid facilitates subsequent chitosan dissolution) under stirring in an 80 °C water bath. After the cloudy white solution turned colorless, chitosan powder was added into the stirring mixture. The final mixture experienced an increase in viscosity as chitosan started to dissolve and required at least 1 hour of stirring in the water bath to obtain a tan colored mixture. The tan mixture was then thinly cast into Petri dishes and sealed in an airtight container. The container was placed in a −20 °C freezer overnight and later removed to thaw at room temperature to complete one freeze–thaw cycle. This process was repeated for three complete freeze–thaw cycles. During each cycle, PVA polymer chains were compressed close together by expanding ice crystals to form junctions *via* hydrogen bonding, eventually resulting in a polymer network (PVA gel trapping chitosan polymer). Meanwhile, ionic cross-linking solution was prepared by dissolving sodium sulfate in Milli-Q water (0.5 M concentration) at room temperature. After the final thaw cycle, an excess amount of cross-linking solution was poured into the Petri dishes ensuring complete coverage of the polymers and allowed to cross-link over 24 hours. At this point, the chitosan network was formed. The Petri dishes were then doubly rinsed with Milli-Q water and immersed in Milli-Q water for 24 hours to remove excess reactants before use in other experiments. Chitosan, acetic acid, and sodium sulfate were excluded in the preparation of PVA SN hydrogel *via* the same freeze thaw protocol. PVA was excluded in the preparation of chitosan SN hydrogel.

2.3. Scanning electron microscopy (SEM)

Hydrogels were flash-frozen in liquid nitrogen and freeze-dried for 72 h to remove all water content. The dried gels were sputter coated with Pd before imaging. Subsurface cross-section imaging was performed in a Hitachi S4800 Scanning Electron Microscope. The imaging parameters were mixed SE detector mode and 10 kV electron beam.

2.4. Energy dispersive spectroscopy (EDS)

Hydrogels were flash-frozen in liquid nitrogen and freeze-dried for 72 h to remove all water content. The dried gels were coated with carbon using a Cressington Carbon Coater 108carbon. Elemental map imaging was performed in a ThermoFisher Axia ChemiSEM. The imaging parameters were Everhart-Thornley SE (ETD) detector mode, spot size 5, 5 kV electron beam, 300 s acquisition time.

2.5. Swelling experiments

Swelling ratios of the hydrogels were calculated by dividing the hydrated weight by the dry weight. Fully hydrated weight refers to the weight of hydrogels that have been equilibrated in solution (water, NaCl, or NaI) until no weight change was observed (*i.e.* 24 hours was sufficient). Dry weight refers to the weight of hydrogels that were dried in an oven at 50 °C for 24 hours. Three replicate hydrogels were examined at each condition.

2.6. Attenuated total reflectance Fourier transform infrared spectroscopy

A Frontier FT-IR spectrometer (PerkinElmer) with diamond head (400–4000 cm^{-1}) was used to characterize the functional groups present on the hydrogels. The reported data are limited to the range of 900–1900 cm^{-1} where the relevant functional groups were identified. The penetration depth of the analysis is approximately ~2 μm, probing into the near surface microstructure.

2.7. Zeta potential measurements

Zeta potentials were measured using SurPASS 3 (Anton Paar). This instrument measures the streaming zeta potential by applying a pressure gradient along a channel between two identical hydrogel films; the streaming current generated by the ion motion is measured and the zeta potential is determined using the Helmholtz-Smoluchowski equation.[28] Two rectangular strips of hydrogel were punched out (standard setup 20 mm × 10 mm for Adjustable Gap Cell provided by Anton Paar) and mounted in the machine with a 100 μm gap between them. Electrolyte solutions at the selected concentrations of NaCl and NaI were then passed through the measuring cell. SurPASS outputs the zeta potential and goodness of fits. Data with goodness $>90\%$ ($n \geq 5$) were averaged and reported.

2.8. Rheology

Rheological measurements were conducted using a parallel-plate rheometer (TA Instruments HR-3). 20 mm diameter by 1 mm thickness circular discs were cut from bulk hydrogels and sandwiched between sandblasted stainless steel parallel plates. Both oscillatory strain and oscillatory frequency measurements were performed at 25 °C, in equilibrium with water and salt solutions (10 mM NaCl and 10 mM NaI). During oscillatory strain measurements, frequency was fixed at 1 Hz while strain varied from 0.01% to 100% (data acquisition stopped at cross-over between G' and G''). A suitable strain value was selected from the linear viscoelastic regime (typically ~0.25%) for use in oscillation frequency measurement. In oscillation frequency measurements, frequency varied from 0.1 Hz to 100 Hz.

2.9. AFM tip preparation

Two types of tips were prepared: blunted and colloidal tips. Blunted tips were prepared by thermally annealing cantilevers with sharp Si tips (Mikromasch HQ:CSC37/No Al) in a tube furnace at 1150 °C for 12 hours. Colloidal tips were prepared by gluing (J-B Weld Epoxy Adhesive 2UV83) silica colloids onto Mikromasch HQ:CSC37 tipless/No Al and the glue was allowed to dry for 24 hours. To do this, a silica colloid dispersion was diluted with Milli-Q water and a drop was poured onto a freshly cleaved mica surface. Water was removed by evaporation on a warm heating plate, leaving the silica colloids on the mica surface. A tungsten wire attached to a microcontroller was used to apply epoxy glue onto tipless cantilevers and a new tungsten wire was used to pick up colloids for attachment. The final tip radius was determined by analyzing topology images in the AFM. By reverse imaging the tips on a calibration standard silica grate, the tip profile was obtained. The apex of the tip profile was then fit with an arc or circle to determine the tip radius.

2.10. AFM measurements

An atomic force microscope (NanoWizard AFM, JPK Instruments) was used for measurements of surface topography, stiffness, adhesion, normal force, and lateral force microscopy. AFM measurements were performed in liquid environment with an in-house membrane cell setup to minimize evaporation. Sader's method[29] was used to determine the normal spring constant. Non-contact thermal noise (JPK Nanowizard) was used for the lateral calibration.[30] Quantitative Imaging (QI) mode (JPK NanoWizard) was used to obtain height difference, stiffness, and adhesion images. QI performs a series of fast force curves at every pixel of the image. It provides simultaneous readings of surface height (topography), stiffness, and adhesion. A small load (10 nN) and very high velocity (250 μm s^{-1}) are applied to reduce viscoelastic deformation so that soft matter interfaces like hydrogels can be imaged.[31,32] Contact mode imaging was used to measure friction. A typical friction measurement involves sliding the AFM tip across the hydrogel surface under a constant load and velocity. These measurements generate height and lateral deflection maps in both trace and retrace directions. By subtracting the lateral deflection (retrace) map from the lateral deflection (trace) map and dividing it by two, and applying the lateral sensitivity and spring constant,[33] a friction image can be generated in Mountains SPIP software (DigitalSurf). This approach enables the direct visualization of the friction force across the hydrogel surface and its comparison to the *in situ* height (topography) images of the sliding contact. This comparison informs about the contact between tip and hydrogel and local deformation of the near-surface hydrogel region. Image processing (image subtraction, line leveling, coloring and scaling) was performed in Mountains SPIP software (DigitalSurf). To quantitatively analyze friction, the friction images were exported into histograms. The significant histogram peaks were deconvoluted by fitting multiple Gaussian distributions and minimized with least squared error. These distributions were then averaged to calculate the mean friction force and standard deviation. Force spectroscopy was used to measure extension and retraction force–distance curves using colloidal and blunted tips. The approach and retract velocities were set at 1 μm s^{-1}, over a total distance of 2 μm. The Hertz contact model was used to determine the elastic moduli of the hydrogels in water, NaCl and NaI solutions from measurements with the colloid using Kaleida Graph software (version 5.0).

2.11. Statistical analysis

SEM and EDS images were obtained from at least two freeze-dried hydrogels. In SEM imaging, at least 5 different magnifications were captured in each location. EDS images were captured from one carbon-coated gel in at least three different locations, and one representative magnification is reported with multiple element display. FTIR data shown are a result of averages over 8 scans per condition. Swelling ratio measurements were performed in triplicate experiments and its average and standard deviation are reported. Rheological measurements were performed on five different hydrogels per condition. Zeta potential measurements were performed in series of 5 measurements per concentration in each solvent and the average and standard deviation at each concentration are reported. AFM nanoscale friction visualization measurements presented in the manuscript were performed on samples from a single parent hydrogel, which was sectioned and equilibrated in different solvent conditions. This approach minimizes the intrinsic variability in hydrogel properties (*e.g.*, surface roughness, water content) as well as variations in tip characteristics (*e.g.*, size, roughness, charge), thereby isolating the effect of fluid composition. Additionally, to assess reproducibility, two additional independent batches of hydrogels were synthesized. In each batch, six hydrogels were prepared, and two independent hydrogels were equilibrated in each solvent condition. Friction measurements are shown in the SI. To enable comparison across different syntheses, friction coefficients and power exponents describing the velocity dependence of friction were compiled. Each friction image covers a 10 × 10 μm area and comprises 256 line scans (QI mode) or 512 line scans (contact imaging mode). Friction data were processed using Mountains® software. Friction histograms from each region were exported as text files and average friction values along with standard deviations were calculated using Microsoft Excel. Error bars represent the standard deviation of the frequency histograms. Force–distance measurements were performed on three hydrogel samples per solvent condition (from different synthesis batches). 20 separate force–distance curves were measured on each hydrogel sample. Average elastic moduli along with standard deviations were calculated using Microsoft Excel.

3. Results

Polyvinyl alcohol/chitosan double network hydrogels were prepared by a two-step cross-linking method, where PVA was cross-linked *via* freeze-thawing and chitosan *via* sulfate anions; sulfate is a divalent anion that can bind to two amine groups in chitosan, providing ionic cross-linking; see synthesis details in Experimental section and Fig. S1. Pure chitosan hydrogels are very soft, but incorporating a double network with PVA significantly enhances their mechanical strength and workability.[1] Energy dispersive spectroscopy (EDS) combined with Scanning Electron Microscopy (SEM) was used to confirm the presence of the two polymers on the surface of the hydrogels; see Fig. 1a and b and SI Text and Fig. S2 and S3 in SI. EDS revealed the presence of sodium on the surface even though the hydrogels were thoroughly rinsed twice with DI water prior to drying. This suggests that a fraction of the sulfate anions does not fully participate in cross-linking amine groups. Instead, they bind to a single amine group, leaving an uncompensated negative charge that is partially screened by sodium ions. The sodium signal is more intense within the clusters located at the junctions of the network, resembling the aggregated microstructure of chitosan SN hydrogels. Hence, they can be cautiously attributed to the higher local concentration of chitosan. The straight strands are reminiscent of the semicrystalline nature of PVA, although significant differences emerge from the synthesis in presence of chitosan; Fig. S2. Infrared spectroscopic characterization also supports the presence of the two polymers near the surface; Fig. 1c and Fig. S1. Altogether, the hydrogels present a surface composed of both PVA and chitosan.

Water and two salt solutions –NaI and NaCl–were selected for measurements. In hydrogels, salts can cause changes in water content or swelling behavior, which in turn can influence properties like adhesion and friction. Fig. 1d shows the negligible change of the swelling ratio of the hydrogels with salt concentration. The swelling ratio of pure PVA hydrogels ($\sim$50) is much higher than that of chitosan hydrogels ($\sim$15), which suggests that chitosan restricts the swelling of PVA. Hydrogels swell when water diffuses into the network, which results from the competition between (i) a free energy of mixing that includes the affinity between the polymer and water and promotes swelling (Π_{mix}), and (ii) the entropy elasticity (Π_{el}), *i.e.* the restoring force against polymer stretching, which counters swelling. Counterions in charged hydrogels introduce the so-called (iii) Donnan osmotic pressure difference (Π_{Do})–due to the different counterion concentration in the gels and in the surrounding environment–which can both promote and reduce swelling. Additionally, (iv) unscreened charges in the network lead to electrostatic repulsion, which promotes swelling (Π_{ch}). The negligible change in swelling ratio indicates a highly entangled structure between the two polymers in the double network.

Although the swelling ratio does not change with salt concentration, the rheological behavior of the hydrogels does, demonstrating the interaction between counterions and polymers; see Fig. 1e and additional experimental results in Fig. S4. The hydrogels behave as viscoelastic solids ($G' > G''$) with a rubbery plateau in the range of frequencies between 0.1 Hz and $\sim$20–30 Hz in water and salt solutions. The loss modulus exhibits only a weak frequency dependence, indicating minimal energy dissipation and suggesting that the physical cross-links remain stable at small deformations under shear. In water, the plateau storage (G') and loss moduli (G'') of the DN hydrogels are 8.9 ± 2.8 kPa and 0.4 ± 0.1 kPa, respectively. These values are higher than those observed in equilibrium with both NaCl and NaI solutions ($G' \sim 7.2 \pm 2.7$ kPa and

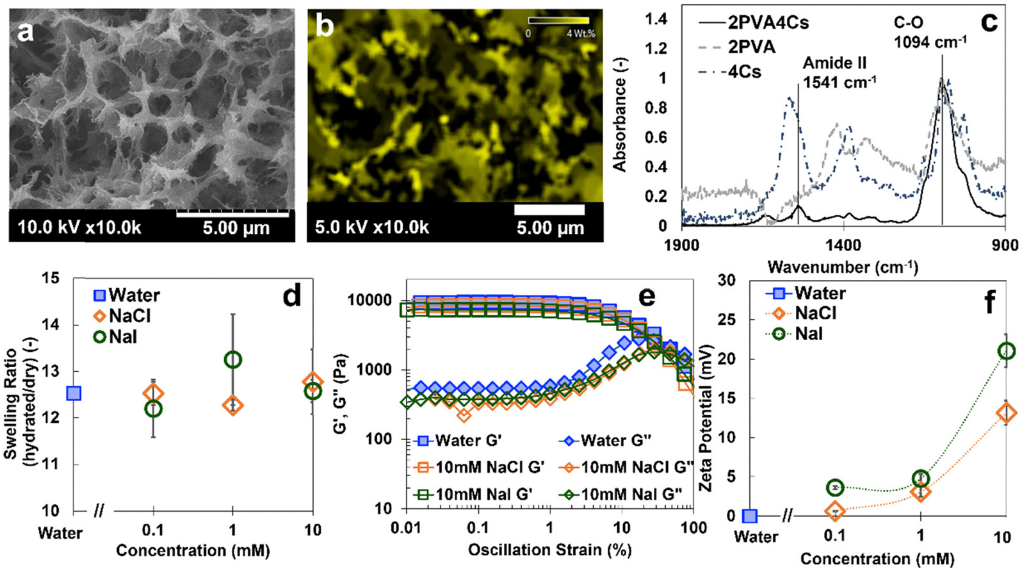

Fig. 1 Hydrogel characterization and responsive properties to added salt. (a) Cross-section SEM image of the DN hydrogel and (b) EDS image of the hydrogel surface; yellow indicates the presence of sodium. (c) Representative ATR-FTIR spectra of SN and DN hydrogels in water; spectra of the hydrogels equilibrated in NaCl and NaI solutions can be found in Fig. S5. (d) Swelling ratio, (e) representative rheological behavior; measurements on more samples are shown in Fig. S4. And (f) zeta potential in function of salt concentration. Colors denote the solvent condition that the hydrogels were equilibrated in, while error bars represent standard deviation.

$G'' \sim 0.2 \pm 0.1$ kPa), indicating that the double network has been partially weakened. FTIR spectroscopy of the hydrogels in 10 mM NaCl and NaI solutions supports that counterions displace sulfate crosslinkers in the chitosan network (Fig. S5).

Surface charge was indirectly compared *via* the zeta potential (ζ) measurements using an electrokinetic streaming method. The zeta potential is measured within the electrical double layer (at the slippage plane) rather than directly at the hydrogel surface. Under conditions of conventional electrostatic screening, the surface charge is expected to have the same sign as the zeta potential.[34] Zeta potential measurements support the hypothesis that chloride and iodide anions partially substitute the sulfate (SO_4^{2-}) cross-linkers and weaken the hydrogel; see Fig. 1f. The ζ value in water is close to zero. Upon addition of 0.1 mM NaCl, ζ increases to $\sim$1 mV and reaches $\sim$13 mV at 10 mM NaCl. Likewise, ζ increases from $\sim$4 mV in 0.1 mM NaI to $\sim$20 mV in 10 mM NaI. Interestingly, the magnitude of ζ in NaI is consistently higher than in NaCl solutions at the same concentration, which may result from differences in the binding affinity of I^- and Cl^- to chitosan. Indeed, the hydration energy of I^- is lower than that of Cl^- (-305 kJ mol^{-1} *vs.* -381 kJ mol^{-1}),[35] which indicates that partial dehydration and substitution of SO_4^{-2} cross-linkers by I^- is energetically more favorable. Sulfates are divalent while chloride and iodide are monovalent, and hence, they cannot bridge two amine groups, justifying the partial weakening of the chitosan network and the increase of its positive charge upon addition of salt.

To further investigate the hydrogel interface, a silica microsphere (radius $R = 2.1$ μm) was glued to the AFM cantilever and used to perform surface force measurements on the hydrogels in a custom-built fluid cell. The surface of the silica microsphere was confirmed to acquire a negative charge in water and in both salt solutions; see Fig. S6.

Fig. 2a and b shows representative force measurements. Fitting the Hertz model to the extension curve at indentation depths of up to 1 μm (black lines), gives elastic moduli of 25.6 ± 7.6 kPa, 20.9 ± 5.6 kPa and 16.4 ± 4.1 kPa, in water, 10 mM NaCl and 10 mM NaI solutions, respectively. The fits deviate from the measurements at low forces, *i.e.*, during compression of the hydrogel's near-surface region, with the discrepancy being much more pronounced in water. The charge of the hydrogel should activate an electrical double layer force,[34] which is attractive due to the opposite charge of hydrogel and tip; see estimation in Fig. S7. This is a rough estimate, since the surface potential is unknown, and it neglects potential charge regulation.[34] Additional contributions are also expected from the dehydration penalty of the confined counter-ions and from the Donnan osmotic pressure difference, however, an estimation is not possible since the counter-ion number density is unknown.

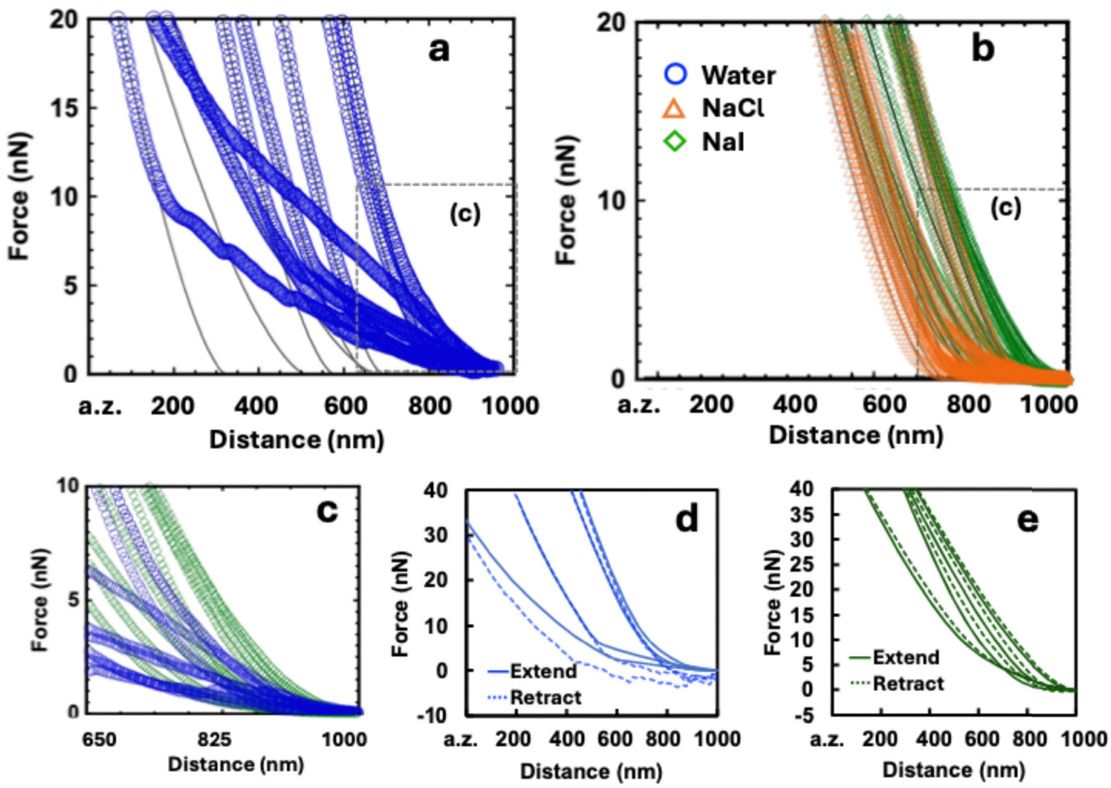

Fig. 2 Force measurements on 2PVA4Chitosan DN hydrogels using a colloid ($R \sim 2$–2.5 μm). Blue circles, orange triangles, and green diamonds represent the results in water, 10 mM NaCl, and 10 mM NaI, respectively. (a) Force–distance curves in water show soft (smaller slope) brush-like region (inset c) followed by stiffer (larger slope) core. (b) Force–distance curves in both 10 mM NaCl and 10 mM NaI lack the near-surface soft region. (c) Zoomed-in plot of initial compression in water and 10 mM NaI. (d) Representative extension and retraction force–distance curves in d, water and e, 10 mM NaI solution. Arbitrary zero abbreviated as a.z.

Notably, the near-surface region of the hydrogel is more readily compressed in water; Fig. 2c. This behavior is attributed to stronger net repulsive interaction between the tip and the hydrogel surface in NaCl and NaI solutions. This repulsive surface force is similar to that measured on polymer thin films and brushes that are either charged and/or hydrophilic, *i.e.* a hydration (polymer-mediated) force.[20,36] Here, such repulsion can arise from PVA being strongly hydrophilic, and therefore, strongly hydrated; in addition to the charged chitosan, which also binds strongly to water. Quantitative modeling of the surface force is not feasible, owing both to the complexity of the superposed interactions and to the unknown absolute surface separation in AFM experiments; labeled as "arbitrary zero" in Fig. 2. Furthermore, the higher variability in force–distance curves in water indicates that the surface is more heterogeneous than in NaCl/NaI solution.

Fig. 2d and e also shows representative force curves upon retraction. In this case, the force–distance curves in water show multiple adhesive detachment events, indicating polymer bridge ruptures as the tip retracts from the surface. The pull-off force is estimated to be around −2 nN, though it is not exact due to the multiple detachment events. In 10 mM NaI and 10 mM NaCl, force–distance curves do not show any adhesion, despite the much higher positive zeta potential. Note that the zeta potential accounts for partial screening of surface charge with the counterions. The negligible adhesion in the salt solution than in water supports the action of a repulsive force that dominates over electrostatic attraction.

Friction force measurements were carried out in water, 10 mM NaCl and 10 mM NaI using colloidal tips. Additionally, a Si tip with a nominal radius of 8 nm was thermally annealed and oxidized, resulting in a blunted tip with cap radius R = 107 nm; Fig. S9. The oxidized tip simulates the surface chemistry of the silica microsphere (*i.e.* SiO_2),[37] while the smaller radius provides higher spatial resolution than the colloid and applies higher pressures; Table S3. The surface of the blunted tip was also confirmed to acquire a negative charge in water and in both salt solutions; see Fig. S6. As with the colloid, retraction force measurements indicate adhesive interactions in water, while no measurable adhesion was observed in NaCl and NaI solutions; Fig. S8. Loads ranging from 10 nN to 50 nN were applied, corresponding to mean Hertzian pressures between ∼4.7 kPa and ∼9.4 kPa when using the colloid, and between ∼39.9 kPa and ∼68.2 kPa, when using the blunted tip, both in water; Table S2 and S3. Cuccia *et al.* have demonstrated that hydrogels deformed to $a_0/R \sim 0.4$ satisfy Hertz contact mechanics.[38]

In contact mode, the AFM tip slides in forward (trace) and reverse (retrace) direction along a scan line at constant load and velocity before moving to the next scan line, producing trace and retrace height (topographic) images of the sliding interface. Due to the friction force between the sphere and hydrogel surface, the cantilever laterally deflects, and trace and retrace lateral deflection images are concurrently generated. Each friction image results from half of the difference between the lateral deflection images in forward and reverse direction multiplied by the lateral spring constant.[33] Comparing friction and topographic images allows us to assess whether the tip probes the polymer network during sliding and deforms it, or loses contact with the surface. Pixel values of all friction images are exported to histograms and fitted by Gaussian distributions to determine the mean friction value and the standard deviation; see details in Materials and methods and SI Text.

Representative friction and topographic images are displayed in Fig. 3 and 4 in function of load and sliding velocity, respectively, while a complete set of images is shown in Fig. S10–S21; note that the color scale of the friction images is the same in all images to facilitate comparison across conditions (see Figure caption). To minimize the variability arising from sample-to-sample differences and examine the influence of the solvent, these friction measurements were performed on multiple pieces sectioned from the same hydrogel sample. First, we describe the results in function of applied load. In water, the colloid appears to track the polymer network and voids (black regions) are visible, where friction is negligible; see also trace and retrace topographic images in Fig. S10. As the load (L) increases to 50 nN, the area covered by voids is reduced, indicating that the tip probes the polymer network better as the pressure increases. The average friction (F) from each image increases linearly from ∼10 pN at L = 10 nN to ∼110 pN at L = 50 nN; Fig. 5a. In 10 mM NaCl, friction is similar at L = 10 nN but there is a noticeable decrease in friction at higher loads, up to a maximum ∼30 pN at L = 50 nN. Similar as in water, the colloidal tip continues to track the polymer network in 10 mM NaCl, but friction images do not change remarkably under an increase in load. In 10 mM NaI, polymer network and voids are not distinguishable, which indicates that the colloidal tip does not track the surface network. This implies that fluid remains between the tip and the hydrogel surface, even under the higher applied load of 50 nN.

With the blunted tip, friction images in water and 10 mM NaCl display a quasi mesh-like pattern, consistent with tracking of the polymer network with higher spatial resolution compared to the colloid. In remarkable contrast, microstructural details are lost in 10 mM NaI, indicating the presence of a fluid film between the tip and the hydrogel surface; see also Fig. S13–S15. Adding salt notably reduces friction at the much higher pressures applied with the blunted tip; Fig. 5c. Note that although the average friction in 10 mM NaCl and 10 mM NaI is similar, the spatial distribution of friction is notably different, and leads to different standard deviations. Friction increases linearly with applied load in the two salt solutions. Deviations from linearity, such as those observed in water, have been reported for hydrogels depending on their composition.[39] Among others, they have been attributed to an increase in adhesion,[24] which is confirmed here, as well; Fig. 2e and f.

We define a friction coefficient as the slope of the linear regression of F *vs.* L, consistent with Amonton's law; Fig. 5a and c. In single-asperity friction measurements, the intercept of the linear regression with the Y-axis is attributed to the contribution of adhesion or stiction to friction.[40] Note that friction is ≈0 at loads smaller than 20 and 30 nN in NaCl and NaI, respectively. Hence, these results indicate the absence of

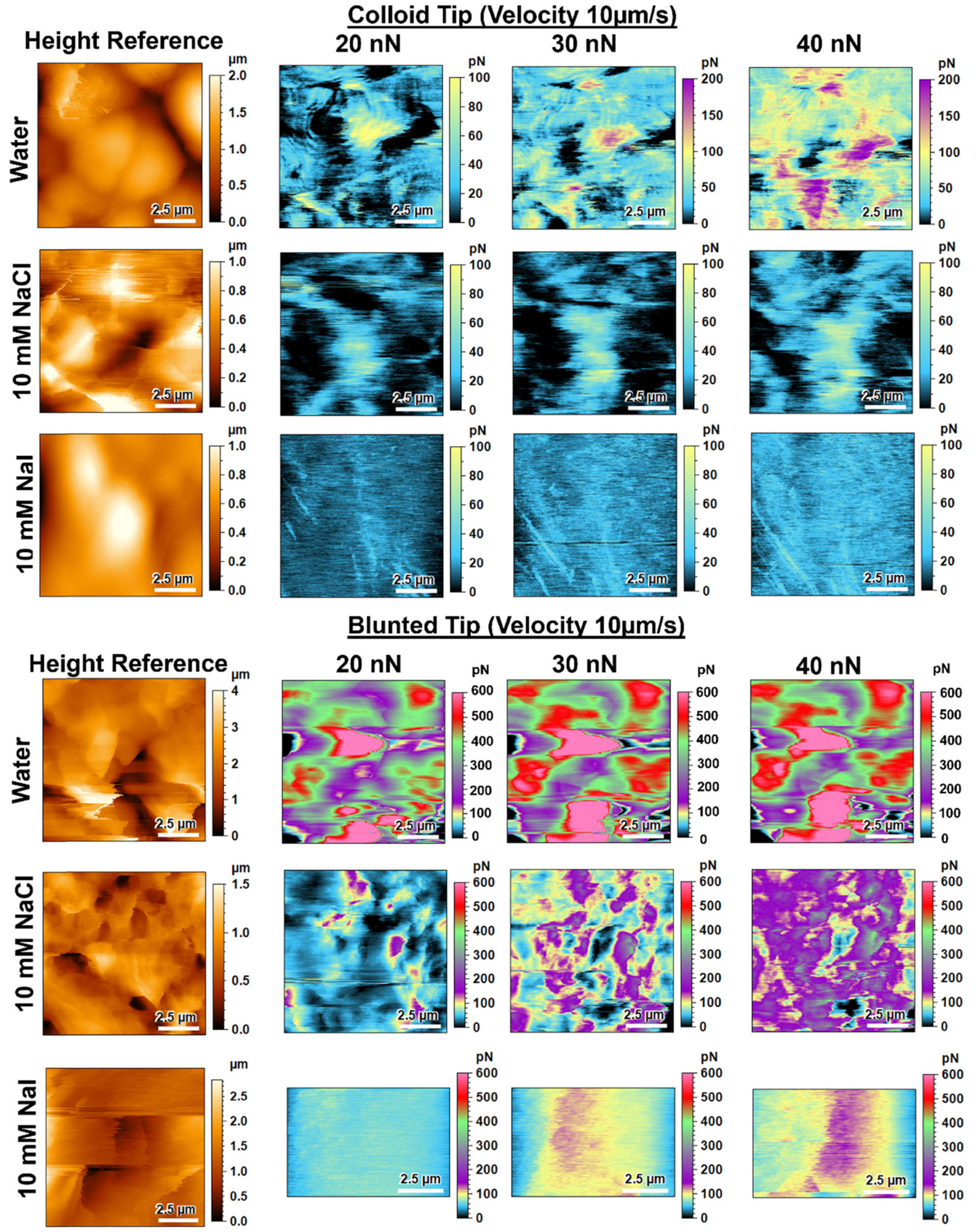

Fig. 3 Topographic and friction images in function of load measured using a silica microsphere (R = 2.1 μm) and a blunted tip (R = 100 nm) at a sliding velocity V = 10 μm s^{-1}. Height reference obtained from quantitative imaging (QI) mode. Color scales of friction are standardized to friction force values, that is, in all friction images blue represents 30 pN, gold 100 pN, purple 200 pN, green 400 pN, and red 600 pN.

stiction despite the opposite charge of the two surfaces. The (low-pressure) coefficient of friction (μ_L) decreases from ≈0.0025 to ≈0.0005, when water is replaced with the salt solution; Fig. 5a. This happens at contact pressures in the range 5.5–9.4 kPa in water and 4.8–8.1 kPa in salt solution; see estimation in Table S2. The high-pressure friction coefficients (μ_H)–as measured with the blunted tip–are greater than μ_L and they remain higher in water compared to salt solution (≈0.0082 in water ≈0.0051 in NaCl and 0.0023 in NaI). This is important because, although the electrostatic (electrical double layer) attraction between the hydrogel and the colloid/tip increases in both salt solutions, friction remains higher in water. Indeed, friction measurements suggest that the interaction between the tip and the hydrogel is more repulsive in NaI solution, when the hydrogels are most positively charged. As inferred from Fig. 2, this can be attributed to a strong net (hydration) repulsion that outcompetes the electrostatic attraction. The decrease in friction with added salts cannot be

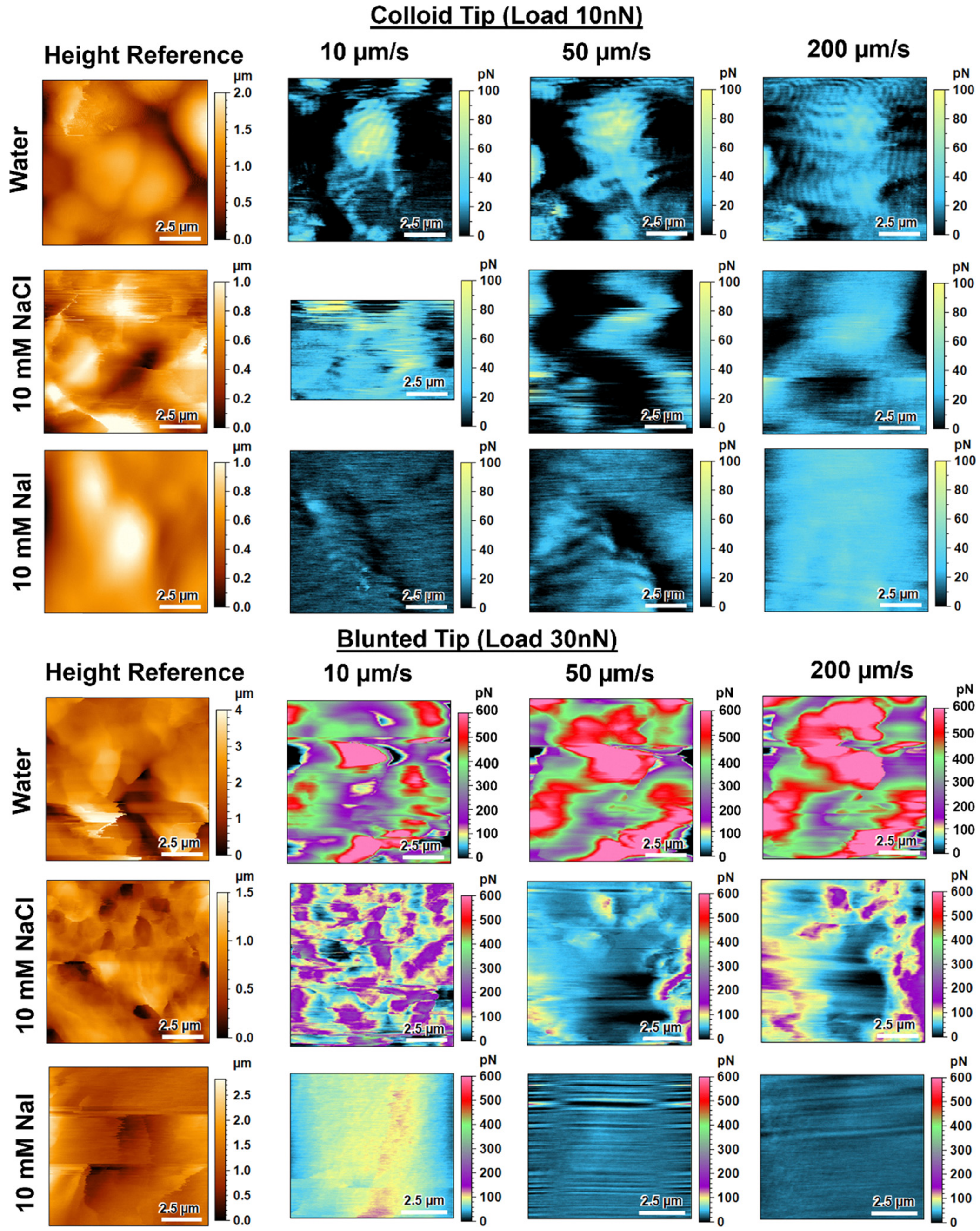

Fig. 4 Topographic and friction images in function of sliding velocities measured using a silica microsphere (R = 2.1 μm) and blunted tip (R = 100 nm) under an applied load L = 10 nN and L = 30 nN respectively. Height reference obtained from quantitative imaging (QI) mode. The friction images obtained with the blunted tip illustrate a case in which the tip is in direct contact with the polymer network in water, as evidenced by the contrast in friction (higher friction on polymer strands and lower friction in the interstitial regions). In contrast, in NaI solution, the tip loses contact, and the friction images become more uniform; see also the height channels in contact mode images (Fig. S16–S21). Color scales of friction are standardized to friction force values, that is, in all friction images blue represents 30 pN, gold 100 pN, purple 200 pN, green 400 pN, and red 600 pN.

accounted for by the decrease in the elastic modulus; see Fig. S22 for details.

A collection of friction coefficients measured on independent hydrogel samples per condition is shown in Fig. 5e. Hydrogels in water have a highly heterogeneous surface structure, with varying thicknesses of the brushy layer as shown in Fig. 2. This greater variability in surface properties in water is reflected in a larger standard deviation in friction coefficient. Despite this, the reduction in friction coefficient upon addition of salt is robust. In contrast, anion-specific effects (Cl^- *vs.* I^-) are smaller than the variability arising from sample-to-sample differences. Such variability is expected in hydrogels and can originate from differences in surface roughness, charge distribution and water content.[41]

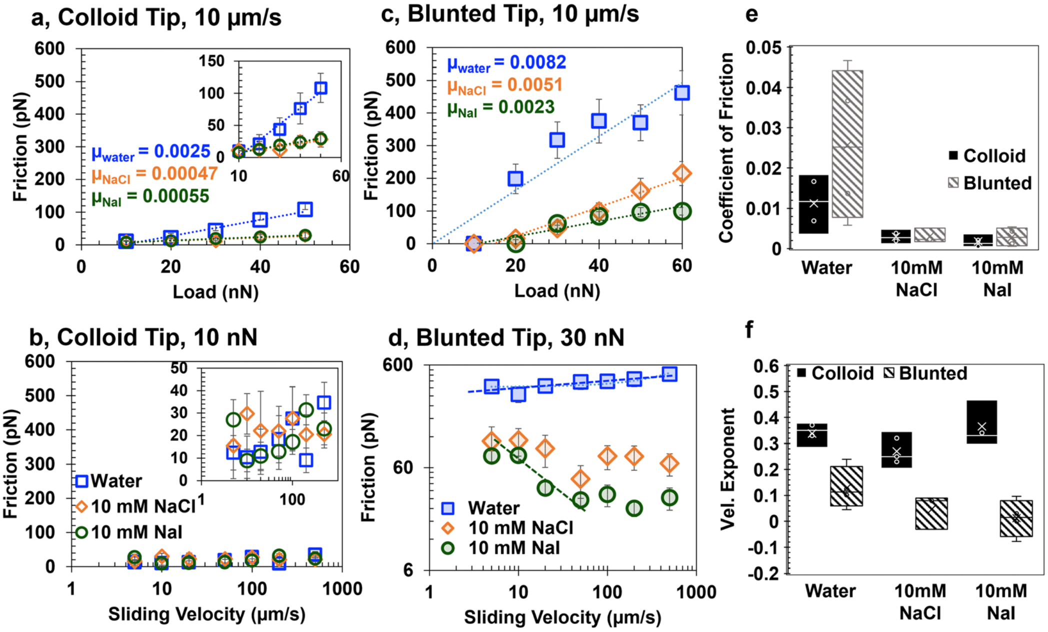

Fig. 5 Average friction extracted from friction images of the hydrogels using a (a) and (b), colloid Fig. S10–S12 and S16–S18) and (c) and (d), blunted tip (Fig. S13–S15 and S19–S21). Load-dependent friction measurements were performed at a sliding velocity of 10 μm s^{-1} and velocity-dependent friction measurements were carried out under an applied load of 10 nN and 30 nN for colloid and blunted tip, respectively. Box-and-whisker plots for the (e), coefficient of friction and (f), power law exponent in the velocity dependence $F \propto V^n$, from measurements on multiple hydrogels.

The velocity-dependence of friction was also studied in the range from 5 μm s^{-1} to 500 μm s^{-1} under an applied load of 10 nN and 30 nN using a colloid and blunted tip, respectively; see full dataset in Fig. S16–S21 and representative results in Fig. 4. Friction images taken with the colloid poorly display the polymer network, indicating that a fluid film remains confined between the hydrogel surface and the colloid. This can also be inferred from the height channel while sliding (Fig. S16–S18). At lower velocities, the tip resolves taller polymer chains and voids resulting in larger height differences. Upon losing contact the tip, a decrease in height difference is observed in trace and retrace topographic images. Under the higher pressures applied by the blunted tip, the polymer network can be clearly resolved in water. In contrast, the blunt tip loses contact with the hydrogel surface above 20 μm s^{-1} in NaCl solution, and already at 10 μm s^{-1} in NaI solution, the most positively charged hydrogel, and despite the negative charge of the tip; see concurrent topographic images in Fig. S19–S21.

Fig. 5b and d shows the average friction (F) as a function of the sliding velocity (V). Under the pressure applied with the colloid (Fig. 5b), the average friction force increases slightly with velocity, remaining within 10–35 pN in all three solutions. We find that $F \propto V^n$, where $n = 0.33$ and 0.38 in water and NaI. The friction force in NaCl seems to be intermediate between the results in water and NaI. Although the standard deviation of the friction measurements is large enough that the data could also be interpreted as velocity-independent, friction measurements on two separate hydrogel samples per solvent condition also display a similar velocity dependence (see Fig. S23, S24 summary of n values in Fig. 5f). Therefore, we assume that this increase in friction with velocity is meaningful, supporting the action of the same underlying lubrication mechanism in water and NaCl/NaI solution if the pressure is sufficiently low.

The decreasing ability to resolve polymer chains and voids in the images with an increase in velocity indicates the presence of a fluid film between the AFM tip and the hydrogel. Furthermore, the fact that hydrogel properties—such as elastic modulus, surface charge (or zeta potential), and the nature of the ions—does not influence the relationship supports that friction is governed by the shear of the fluid. Soft EHL (eqn (1)) predicts $F \propto V^{0.35}$, which is close to the fitting parameter, n, (0.33–0.38 in Fig. 5b and 0.36 ± 0.04 in Fig. 5f). The contact area (A) for eqn (1) was estimated based on the Hertz model for small elastic deformation; see details in Table S2. This model neglects viscoelastic deformation of the hydrogel, which is a reasonable approximation based on its rheological behavior under small strains (Fig. 1e). Eqn (1) estimates a film thickness (h) between 2 nm and 30 nm at 10 and 500 μm s^{-1}, respectively, which is smaller than expected based on classical EHL theory. That is, a nanoscopic fluid film—arising from hydration repulsion and consistent with the concept of hydration lubrication—lubricates the contact under small pressures and substantially reduces friction ($\mu_L < 0.01$), yet exhibits a non-negligible velocity dependence due to the shear of the confined fluid. This analysis assumes that water remains Newtonian and low viscosity (1 mPa s). While this assumption is supported by several studies,[5,42] deviations have been also reported: water exhibits viscoelastic behavior under extreme confinement ($h < 1.0$ nm),[43,44] and high shear rates (from 10^4 to 10^5 s^{-1}) and oscillation frequencies (5–25 kHz).[45] In the present system, the compliant nature of the hydrogel and the comparatively lower frequencies (few Hz) suggest that such conditions are unlikely to be reached.

Concurrently with the increase in the friction coefficient (μ_L up to $\sim$0.045, Fig. 5e) when the blunted tip slides on the hydrogel in water under high pressure, friction gradually increases with sliding velocity according to $F \propto V^n$, where $n \sim 0.1$ in Fig. 5d ($n \sim 0.12 \pm 0.08$ in Fig. 5f). An estimate of the film thickness based on soft EHL (eqn (1)) for hydrogels in water leads to unreasonably small values of the fluid film ($h \sim 0.017$ nm). Friction and topographic images (Fig. 4 and Fig. S19) support the direct contact between the tip and the polymer network, and therefore the absence of a fluid film. As detailed in the SI Text, an adhesive friction model[17] also fails to describe the increase in friction with velocity (Fig. S25).

Hydrogels are poroelastic, and as such pressure-driven fluid flow occurs when the applied pressure exceeds the osmotic pressure of the hydrogel. The osmotic pressure of a polymer swollen in equilibrium with a good solvent is close to the shear storage modulus.[46] Under the colloid, the estimated mean pressure in water and salt solutions is lower than the hydrogel's shear modulus, suggesting that fluid drainage does not occur; Table S2.[46] However, under the load applied by the blunted tip, the estimated mean pressure is higher than the hydrogel's shear modulus (Table S3). This suggests that fluid drainage does occur, if the contact time a/V is greater than the poroelastic relaxation time, τ_W, which characterizes the pressure-driven fluid flow. Based on the Darcy's law, τ_W can be roughly estimated from $\tau_w = \dfrac{6\eta_s \pi a^2}{P\xi^2}$ as a function of mesh size ξ, pressure P, contact radius a, and solvent viscosity η_s ($\sim$1 mPa s). Table S3 estimates the contact mechanics parameters for a blunted tip of different geometries. For example, for a paraboloid shape, under a load of 30 nN, it yields $a = 0.41$ µm. The mesh size of the hydrogels is $\xi \sim 1$ µm (from AFM images), which leads to relaxation times $\tau_W \sim 0.054$ µs, much smaller than the contact times, a/V (0.04–0.0008 s), yielding Peclet numbers smaller than 1. There could be a small mesh size that was not visualized in SEM or AFM images, but the largest mesh size will dominate the fluid flow.

Based on the above estimation, poroelastically-driven lubrication is possible.[24,46–48] Delavoipière *et al.*[23] used crack growth theory to derive a simple equation for the friction force in function of the poroelastic relaxation time. If $\tau_w < \dfrac{a}{V}$, then

$$F \sim F_0 + \frac{\sqrt{2}}{3} L (\tau_0 V / a)^{0.5} \tag{2}$$

This model fits the experimental results in water very well ($R^2 = 0.976$, see dashed line in Fig. 5d), considering a low-velocity (static) friction F_0, with a fitting parameter $\tau_0 \sim 0.07$ µs, which is a bit larger than the estimated value above. An increase in the viscosity of water under confinement by a factor of 1.5 at most according to ref. 42 or a slightly smaller mesh size would yield a poroelastic relaxation time closer to τ_0. The satisfactory agreement between the model parameter and the estimated relaxation time supports the relevance of poroelastically-driven lubrication in this case.

In NaCl and NaI solutions, friction decreases with velocity before leveling off to an approximately constant value, much smaller than in water; Fig. 5d. As described in the Introduction, a decrease in friction with velocity may originate from poroelastically-driven lubrication, if the contact area decreases with increasing velocity.[23] However, this requires Peclet numbers greater than 1, which are not reached under the conditions of these experiments $\left(\tau_w \ll \dfrac{a}{V}\right)$, and therefore, we can exclude poroelastic-driven lubrication in this case. A decrease of friction with increasing velocity can also result from adhesive-dominated friction, either due to an increased interfacial hydration[24] and/or from a reduced interfacial strength,[12] since bonds between the sliding surfaces cannot form as fast. It is possible that the negative charges on the tip attract positive groups in chitosan at sufficiently slow velocities. However, we refrain from fitting this model to our results because the number of data points is too small, and the contact geometry between the blunted tip and the hydrogel is too complex to be modeled precisely.

More notable is the following quasi plateau ($n \sim 0.04 \pm 0.09$), which correlates with the absence of direct contact between the blunted tip and the hydrogel network in friction images; Fig. S20 and S21. At $V_c \sim 100$ µm s^{-1}, the friction force at small and high pressures in salt solutions reaches approximately the same level, pointing at similar mechanisms. As with the colloid, we propose this is the onset of hydration lubrication, but it is only achieved under high pressure if salt is added to the system. Based on the results from force measurements (Fig. 2), we invoke the action of a strong repulsion that surpasses the effect of the electrostatic attraction and the applied pressure. Such repulsive interaction can thus be justified by (i) the hydrophilic nature of PVA, (ii) the enhanced charge of the hydrogels in salt solution, which binds more water and raises the dehydration penalty under compression,[49] and (iii) the Donnan osmotic pressure difference introduced by the higher concentration of counterions at the interface compared to the surrounding solution.

4. Discussion

In summary, this study reveals that, despite enhanced electrostatic attraction to the countersurface, the hydrogels become more lubricious in NaCl and NaI solutions. We thus propose that hydrogel charging strengthens hydration repulsion, thereby reducing the friction coefficient to levels characteristic of superlubricity; see Fig. 6. The concurrent visualization of friction and contact topography upon sliding–including loss of contact–, together with the reduced resistance to compression of the near-surface region, supports the presence of a thin fluid film that efficiently lubricates the interface. This interpretation is partially based on estimates of the fluid film thickness using soft EHL theory (eqn (1)) in combination with Hertzian contact mechanics. These estimates remain approximate, as

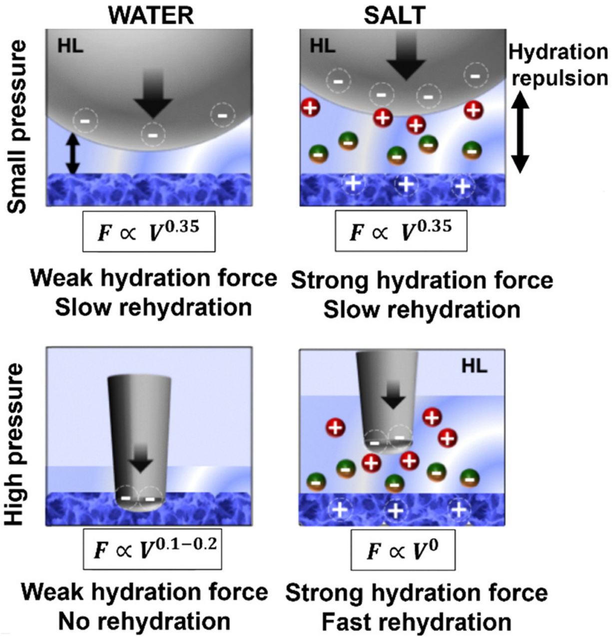

Fig. 6 Proposed mechanisms of lubrication. HL denotes hydration lubrication, which occurs with the colloid in water and salt solution, and with the blunted tip in the presence of the salt solution.

the hydrogel is not only soft but also poroelastic. Neutron reflectometry (NR) has been used to measure the thickness of hydrated polymer thin films,[50] and more recently, to probe the hydration layer between (brush-terminated *vs.* well-crosslinked) polyacrylamide hydrogels and rigid countersurfaces under a static loading.[20] Therefore, NR represents a promising technique to directly quantify the thickness of the hydration layer on double-network hydrogels under sliding conditions, which we propose to explore in future work. Extensions of sum-frequency generation (SFG)[51] to study hydrogels—particularly under simultaneous compression and sliding—could also be useful in future studies.

The quasi velocity independence of the friction force measured with the blunted tip, in contrast to the velocity-dependent behavior with the colloid probe, is intriguing, given that both are governed by lubrication through a nanoscopic fluid film–originating from hydration forces–that prevents direct contact between the polymer network and the rigid probe. A recent study by Klein *et al.* attributed the velocity-dependence of friction to the crosslinking characteristics of the interface.[9] Specifically, at brushier (*vs.* more crosslinked) interfaces, self-regulating interpenetration of opposing polymer chains at higher sliding velocities can offset increased energy dissipation, resulting in a weaker dependence of friction on velocity. In the hydrogel-tip configuration, however, an interpenetration zone is not possible, and velocity-independent friction is observed only with the blunt tip. This suggests a different mechanism governing the regulation of the film thickness. We posit that the smaller contact area between the blunted tip and the hydrogel surface enhances rehydration (*i.e.* the increase in film thickness h with velocity) during sliding relative to the colloidal tip, for the same molecular relaxation process, provided that the hydration repulsion exceeds the applied pressure. This mechanism can account for the observed plateau with the blunted tip, ($F \propto V/h \sim V^0$), in contrast to the power law measured with the colloid ($F \propto V^{0.35}$). At sufficiently high sliding velocities, a transition to velocity-dependent friction may be expected even for the blunted tip; however, such a transition is not observed within the experimental range explored here (up to 500 μm s^{-1}).

It is possible to estimate the energy required for the dehydration of the protonated amines in chitosan and PVA to support the mechanism of hydrogel hydration lubrication. The dehydration penalty of the hydroxyl groups in PVA should contribute to the repulsive interaction between tip and hydrogel interface. Taking the hydration enthalpy of vinyl alcohol (VA), $\Delta H_{\text{hyd}} \approx -30$ kJ mol^{-1} (ref. 52) and the VA concentration per unit volume in the hydrogels (c = 454.5 mol m^{-3}), yields a dehydration penalty within a slab of ∼0.4 nm (size of VA) in thickness equal to $E_{\text{hyd}} \approx 0.00544$ J m^{-2}. Applying the Derjaguin approximation, the corresponding repulsive barrier or force can be estimated from $F^{\text{w}}_{\text{hyd}} = 2\pi R E_{\text{hyd}}$ and it is $F^{\text{w}}_{\text{hyd}} \approx$ 68.4 nN in the case of the colloid, which is higher than the applied force in our experiments, supporting the action of a strong hydration repulsion (i). While this is only a rough estimation, it indicates that the order of magnitude of the hydration repulsion is relevant to the forces applied in AFM experiments.

Adding salt activates an additional dehydration penalty (ii). The effective surface charge density σ_{eff} of the hydrogels is related to the surface potential ϕ_0 by the Grahame equation.[34] Since ϕ_0 is unknown, we use the zeta potential ζ to get a rough estimate of σ_{eff},[53]

$$\sigma_{\text{eff}} \sim \sqrt{8cN_{\text{A}}\varepsilon T}\sinh\left(\frac{e\zeta}{2k_{\text{B}}T}\right) \qquad (3)$$

where c is the counterion concentration, N_{A} the Avogadro constant, k_{B} Boltzmann's constant, ε the permittivity of water, and T the temperature. Taking ζ = 20 mV in 10 mM NaI solution yields $\sigma_{\text{eff}} \sim 4.74$ mC m^{-2}. The number of protonated amine groups per unit area is $n = \sigma_{\text{eff}}/q_{\text{e}}$, and the energy per unit area required for their dehydration is equal to $E_{\text{hyd}} = n\Delta H_{\text{hyd}}/N_{\text{A}}$. Taking the hydration energy of protonated amines (NH_4^+) as $\Delta H_{\text{hyd}} = -166$–$305$ kJ mol^{-1} (ref. 35 and 54) leads to E_{hyd} = 0.0082–0.0152 J m^{-2}. Such energy penalty would result in a repulsive force–a hydration force–against the applied load and the electrostatic attraction. Applying the Derjaguin approximation, the hydration repulsion can be estimated from $F^{\text{s}}_{\text{hyd}} = 2\pi R E_{\text{hyd}}$ and it is ≈100–185 nN in the case of the colloid. The overall repulsive interaction upon addition of salt results from $F_{\text{hyd}} = F^{\text{w}}_{\text{hyd}} + F^{\text{s}}_{\text{hyd}}$. Despite these simplifications, the stronger repulsion estimated in NaI solution compared with water is, indeed, consistent with the lower friction coefficients in salt solution and AFM images showing that the blunted tip cannot approach the surface of the hydrogel.

When comparing measurements performed on the same hydrogel sample (Fig. 5a–d), hydration lubrication is most effective in NaI solution, revealing subtle anion-specific effects. Based on the considerations above, the smaller magnitude of ζ in NaCl relative to NaI is expected to result in weaker hydration repulsion and a lower osmotic pressure associated with Cl^- counterions. This provides a rationale for why the tip can approach closer to the hydrogel surface in NaCl than in NaI, as inferred from AFM images.

Fig. 5e and f compares friction coefficients (μ_L and μ_H) and power-law exponents (n) obtained from measurements across different hydrogel samples using multiple tips. While the coefficient of friction is consistently lower in salt solutions than in water, the standard deviation arising from sample-to-sample variability exceeds the effect of the salt composition. Consequently, variations in surface properties among different hydrogel samples obscure the anion-specific effects. The freeze-thawing method to synthesize physically crosslinked PVA-based gels commonly results in a highly heterogeneous surface due to ice crystal formation and melting, creating heterogeneous PVA crystallite distribution and asymmetric large pores during thawing.[55] The combination of these processes can result in highly rough and porous hydrogel surface.

Long-term stability is critical for the application of PVA-based hydrogels. Previous studies have reported an initial dissolution of the PVA phase and melting of crystallites over time, followed by recrystallization upon aging, which can lead to solvent exclusion.[56] In the investigated double-network hydrogels, chitosan was shown to substantially influence the microstructure, including the formation and stability of PVA crystallites, and may therefore enhance long-term stability. While the conclusions presented here are robust for hydrogels investigated up to 3 weeks after synthesis, the long-term stability and potential wear under extended tribological loading (*e.g.*, hundreds to thousands of cycles) have not yet been evaluated and remain important directions for future investigation.

5. Conclusion

In conclusion, this work has investigated the lubrication of hydrogels composed of PVA and chitosan, whose charge become increasingly positive with concentration of NaCl and NaI solutions. Despite the enhanced electrostatic attraction to the countersurface, the hydrogels become more lubricious. Here, it is proposed that the charging of the hydrogel leads to a stronger hydration repulsion that activates hydration lubrication, reduces the friction coefficient to levels characteristic of superlubricity and results in a different velocity-dependence of friction depending on the contact size in the same range of sliding velocities and loads. More broadly, this study reveals how charged hydrogels can be engineered to remain lubricious even against oppositely charged surfaces. Many stimulus-responsive hydrogels possess charged functional groups, relying on coulombic interactions for attraction (adhesion) or repulsion (lubricity) against countersurfaces.[57,58] The current work demonstrates that polymer hydration can counteract the electrostatic attraction between oppositely charged hydrogel-solid surfaces. This shows the surprising ability for thin hydration layers to overcome the influence of longer-range electrostatic interaction, and it is particularly important in biomedical applications because many tissues, like cartilage or corneal epithelium,[9] are charged. The findings of this work open questions regarding the limits of attractive/adhesive interactions for future consideration.

Author contributions

Ming Jun Lee (first author): conceptualization, investigation, data curation, methodology, software, visualization, writing – original draft, writing – review & editing. Isha Bordawekar: methodology, investigation, visualization. Rosa M. Espinosa-Marzal (corresponding author): conceptualization, writing – original draft, writing – review & editing, funding acquisition, methodology, supervision, project administration.

Conflicts of interest

There are no conflicts to declare.

Data availability

The original data are available from the corresponding author upon reasonable request.

The data supporting this article have been included as part of the supplementary information (SI). Supplementary information is available. See DOI: https://doi.org/10.1039/d5mh02460a.

Acknowledgements

This article is based on work supported by the National Science Foundation under grant CMMI 2154530. Research was carried out in part in the Materials Research Laboratory Central Research Facilities, University of Illinois. We thank Dr Thomas Luxbacher for guidance in optimizing zeta potential measurements with the SurPASS 3 instrument. The authors are thankful to George Heintz for the artwork of table of contents/Fig. 6.

References

1 R. Carpa, A. Farkas, C. Dobrota and A. Butiuc-Keul, *Gels*, 2023, 9.
2 Z. Gu, K. Huang, Y. Luo, L. Zhang, T. Kuang, Z. Chen and G. Liao, *Wiley Interdiscip. Rev.: Nanomed. Nanobiotechnol.*, 2018, **10**, e1520.
3 Y. Lee, W. J. Song and J. Y. Sun, *Mater. Today Phys.*, 2020, 15.
4 L. Li, P. Wu, F. Yu and J. Ma, *J. Mater. Chem. A*, 2022, **10**, 9215–9247.
5 U. Raviv and J. Klein, *Science*, 2002, **297**, 1540–1543.
6 H. Shekhar and R. Dumpala, *Appl. Surf. Sci. Adv.*, 2021, 6.
7 U. Raviv, S. Giasson, N. Kampf, J. F. Gohy, R. Jerome and J. Klein, *Nature*, 2003, **425**, 163–165.

8 M. Chen, W. H. Briscoe, S. P. Armes, H. Cohen and J. Klein, *Eur. Polym. J.*, 2011, **47**, 511–523.

9 W. Lin and J. Klein, *Acc. Mater. Res.*, 2022, **3**, 213–223.

10 W. Lin, M. Kluzek, N. Iuster, E. Shimoni, N. Kampf, R. Goldberg and J. Klein, *Science*, 2020, **370**, 335–338.

11 Z. Li, Q. Liu, Q. Li and M. Dong, *Nano Res.*, 2022, **16**, 1096–1100.

12 J. Gong and Y. Osada, *J. Chem. Phys.*, 1998, **109**, 8062–8068.

13 G. Kagata, J. P. Gong and Y. Osada, *J. Phys. Chem. B*, 2002, **106**, 4596–4601.

14 B. J. Hamrock and D. Dowson, *J. Lubric. Tech.*, 1978, **100**, 236–245.

15 J. K. Martin and D. W. Parkins, *J. Tribol.*, 2002, **124**, 203–211.

16 A. A. Pitenis, J. M. Uruena, K. D. Schulze, R. M. Nixon, A. C. Dunn, B. A. Krick, W. G. Sawyer and T. E. Angelini, *Soft Matter*, 2014, **10**, 8955–8962.

17 T. Shoaib and R. M. Espinosa-Marzal, *Tribol. Lett.*, 2018, 66.

18 R. Simič, M. Yetkin, K. Zhang and N. D. Spencer, *Tribol. Lett.*, 2020, 68.

19 J. P. Gong, Y. Iwasaki, Y. Osada, K. Kurihara and Y. Hamai, *J. Phys. Chem. B*, 1999, **103**, 6001–6006.

20 Y. Gombert, R. Simic, F. Roncoroni, M. Dubner, T. Geue and N. D. Spencer, *Adv. Mater. Interfaces*, 2019, 6.

21 J. M. Urueña, A. A. Pitenis, R. M. Nixon, K. D. Schulze, T. E. Angelini and W. G. Sawyer, *Biotribology*, 2015, **1**, 24–29.

22 A. Deptula and R. M. Espinosa-Marzal, *Adv. Funct. Mater.*, 2025, **36**, e11763.

23 J. Delavoipiere, Y. Tran, E. Verneuil, B. Heurtefeu, C. Y. Hui and A. Chateauminois, *Langmuir*, 2018, **34**, 9617–9626.

24 E. R. Reale and A. C. Dunn, *Soft Matter*, 2017, **13**, 428–435.

25 L. Ding, Y. Huang, X. Cai and S. Wang, *Carbohydr. Polym.*, 2019, **208**, 133–141.

26 J. P. Gong, Y. Katsuyama, T. Kurokawa and Y. Osada, *Adv. Mater.*, 2003, **15**, 1155.

27 P. Calvert, *Adv. Mater.*, 2009, **21**, 743–756.

28 A. Yaroshchuk and T. Luxbacher, *Langmuir*, 2010, **26**, 10882–10889.

29 J. E. Sader, J. W. M. Chon and P. Mulvaney, *Rev. Sci. Instrum.*, 1999, **70**, 3967–3969.

30 N. Mullin and J. K. Hobbs, *Rev. Sci. Instrum.*, 2014, **85**, 113703.

31 M. J. Lee and R. M. Espinosa-Marzal, *ACS Appl. Mater. Interfaces*, 2023, **15**, 20495–20507.

32 M. J. Lee, D. R. Shrotriya and R. M. Espinosa-Marzal, *Adv. Funct. Mater.*, 2024, **34**, 2402279.

33 R. W. Carpick and M. Salmeron, *Chem. Rev.*, 1997, **97**, 1163–1194.

34 J. N. Israelachvili, *Intermolecular and surface forces*, Academic press, 2011.

35 D. W. Smith, *J. Chem. Educ.*, 1977, **54**, 540.

36 J. Klein, Y. Kamiyama, H. Yoshizawa, J. N. Israelachvili, G. H. Fredrickson, P. Pincus and L. J. Fetters, *Macromolecules*, 2002, **26**, 5552–5560.

37 K. H. Chung, Y. H. Lee and D. E. Kim, *Ultramicroscopy*, 2005, **102**, 161–171.

38 N. L. Cuccia, S. Pothineni, B. Wu, J. Mendez Harper and J. C. Burton, *Proc. Natl. Acad. Sci. U. S. A.*, 2020, **117**, 11247–11256.

39 J. P. Gong, *Soft Matter*, 2006, **2**, 544–552.

40 C. M. Mate and R. W. Carpick, *Tribology on the Small Scale*, Oxford University Press, 2019.

41 M. V. Flores-Merino, S. Chirasatitsin, C. Lopresti, G. C. Reilly, G. Battaglia and A. J. Engler, *Soft Matter*, 2010, **6**, 4466–4470.

42 U. Raviv, P. Laurat and J. Klein, *Nature*, 2001, **413**, 51–54.

43 T. D. Li and E. Riedo, *Phys. Rev. Lett.*, 2008, **100**, 106102.

44 S. H. Khan and P. M. Hoffmann, *Phys. Rev. E:Stat., Nonlinear, Soft Matter Phys.*, 2015, **92**, 042403.

45 K. Kapoor, Amandeep and S. Patil, *Phys. Rev. E:Stat., Nonlinear, Soft Matter Phys.*, 2014, **89**, 013004.

46 E. Geissler, A. M. Hecht, F. Horkay and M. Zrinyi, *Macromolecules*, 1988, **21**, 2594–2599.

47 K. D. Schulze, S. M. Hart, S. L. Marshall, C. S. O'Bryan, J. M. Urueña, A. A. Pitenis, W. G. Sawyer and T. E. Angelini, *Biotribology*, 2017, **11**, 3–7.

48 T. Shoaib and R. M. Espinosa-Marzal, *Colloids Interfaces*, 2020, 4.

49 Z. Zachariah, M. P. Heuberger and R. M. Espinosa-Marzal, *One Hundred Years of Colloid Symposia: Looking Back and Looking Forward*, American Chemical Society, 2023, vol. 1457, ch. 2, pp. 31–47.

50 T. Ederth and T. Ekblad, *Langmuir*, 2018, **34**, 5517–5526.

51 H. Noguchi, M. Hiroshi, T. Tominaga, J. P. Gong, Y. Osada and K. Uosaki, *Phys. Chem. Chem. Phys.*, 2008, **10**, 4987–4993.

52 R. Kurapati and U. Natarajan, *Ind. Eng. Chem. Res.*, 2020, **59**, 16099–16111.

53 Z. Ge and Y. Wang, *J. Phys. Chem. B*, 2017, **121**, 3394–3402.

54 M. Liu, Q. Shi and Z. Sun, *Nano Express*, 2022, **3**, 045005.

55 F. Soto-Bustamante, G. Bassu, E. Fratini and M. Laurati, *Gels*, 2023, 9.

56 C. M. Hassan and N. A. Peppas, *Macromolecules*, 2000, **33**, 2472–2479.

57 A. Deptula, J. Rangel-Galera and R. M. Espinosa-Marzal, *Adv. Funct. Mater.*, 2023, 33.

58 A. Deptula, M. Wade, S. A. Rogers and R. M. Espinosa-Marzal, *Adv. Funct. Mater.*, 2021, 32.